Supporting Information

Subnano confinement in robust MoS_2-based membranes for high-performance osmotic energy conversion

Xuying Wang [a#], Zhaoyi Wang [a#], Zhiwei Xue [a], Yiyi Fan [a], Jing Yang [a], Qingxiao Zhang [a], Naitao Yang [a,], Xiuxia Meng [a,*], Yun Jin [a], Shaomin Liu [b,*]*

Experimental Section

1 Materials

Molybdenum trioxide (MoO_3, AR, 99.5%), urea (CH_4N_2O, AR, 99%), thioacetamide (C_2H_5NS, AR, 99%) were obtained from Shanghai Macklin Biochemical Co., Ltd (China). Bacterial nanocellulose (BNC, 0.8%) dispersions were provided by Guilin Qihong technology Co. Ltd. Nylon filter film (pore size ~0.2μm) was purchased from Whatman. Potassium chloride (KCl, AR, 99.5%), sodium chloride (NaCl, AR, 99.5%), lithium chloride (LiCl, AR, 99%), magnesium chloride ($MgCl_2$, AR, 98%) and calcium chloride ($CaCl_2$, AR, 96%) were provided by Sinopharm Chemical Reagent Co. Ltd. All chemicals were used without further purification.

2 Fabrication of MoS_2/BNC composite membrane

MoO_3 (1.2 g), thioacetamide (1.4 g) and urea (10 g) were firstly dissolved in deionized water (100 mL), and then BNC was added into the solution following continuous stirring for 2 h. Then the mixed solution was transferred into a Teflon-lined autoclave and heated to 200 ℃ for 20 h. After the completion of the reaction, the prepared MoS_2/BNC mixture was centrifuged and washed thoroughly in sequence with ethanol and deionized water until to pH reaching 7. The resultant MoS_2/BNC composite was exfoliated under ultrasonication and continuous stirring to obtain nanosheets in monolayer or several layers. After removing unexfoliated MoS_2/BNC by centrifugation, a stable colloidal solution with 1 mg/mL MoS_2/BNC nanosheets was obtained for the membrane preparation. The MoS_2/BNC composite membrane supported by the hydrophilic nylon filter was prepared using vacuum-assisted filtration method schematically shown in Figure S1. Nylon filtration mesh (diameter: 50 mm; thickness 0.1 mm) with pore size of ~0.2 μm microns (Figure S6) was used as the substrate to assemble the MoS_2/BNC nano sheets. The applied stable colloidal solution (50 mL) with concentration of 0.05 mg (MoS_2/BNC) per mL was filtrated and

assembled on the nylon mesh via vacuum operation. The vacuum time for the preparation of 300-600 nm thick membrane was about 10-20 minutes. Vacuum drying at 40 ℃ for 5 h after the successful preparation of nylon supported composite membrane. The large membrane was cut into small membranes with diameter around 3 mm to be applied for subsequent osmotic energy conversion. For comparison, pure MoS_2 laminar membrane were also prepared by similar method.

The weight content (ω) of BNC in the MoS_2/BNC composite membranes were determined by thermogravimetric analysis (TGA, SDT650) based on Equation (S1):[1]

$$\omega=\frac{M_{MoS_2/BNC}-M_{MoS_2}}{M_{BNC}-M_{MoS_2}} \quad \text{(S1)}$$

Where $M_{MoS2/BNC}$, M_{MoS2}, M_{BNC} represent the weight loss of MoS_2/BNC, MoS_2 and BNC between 150 ℃ and 600 ℃, respectively.

3 Characterization

The microtopography of the MoS_2 and MoS_2/BNC membrane were detected by field-emission scanning electron microscopy (FESEM, FEI Quanta 250) and transmission electron microscopy (TEM, Tecnai G2 F20 S-TWIN). X-ray diffraction (XRD) patterns were collected in a Bruker D8 Advance with Cu-Kα radiation. The Fourier transform infrared spectroscopy (FT-IR, Nicolet 5700) was employed to investigate the chemical compositions of the as-prepared materials. X-ray photoelectron spectroscopy (XPS, ESCALAB 250Xi) was collected spectra on an Al Kα source and was applied to determine the surface chemical states and phase ratios of the as-synthesized MoS_2. Raman spectra were collected in a WJGS-034 Raman microscope. The surface charge of MoS_2/BNC composite membranes were measured by the static water contact angles system (SZ-CAMC13). The BNC mass content in MoS_2/BNC composite membrane was measured by thermal gravimetric analysis (TGA, SDT650). Numerical and Density functional theory (DFT) simulation are shown in Supporting information, detailly. The degree of interfacial adhesion between the impregnated MoS_2 and the support was determined by a scratch test using a nanoindenter (NanoTest™ Vantage). The size of MoS_2 nanosheets was detected using AFM (Veeco Multimode Ns3a, America).

4 Electrical measurement

Ion transport properties and osmotic energy conversion test of BNC/MoS_2 composite membranes were conducted using an electrochemical workstation (CHI660e, Chenhua Instrument Co., Ltd.). The composite membrane was installed between two conductance cells. The artificial river (0.01 M NaCl) and simulated sea water (0.5 M NaCl) were placed in two separated electrochemical cells, respectively. A pair of homemade Ag/AgCl electrodes was used to apply transmembrane electrical potential (Figure S15). The effective test area (*S*) of

MoS_2/BNC composite membranes were about 0.78 mm^2, which is about 20 times of the common testing area of 3×10^4 μm^2. All testing electrolytes were prepared using deionized water, and the pH value was adjusted using HCl and/or NaOH solutions. To further show promising application, the seawater from Yellow sea in Tsingtao and the river water from Jixia lake in Shandong University of Technology have also used as electrolyte solution for testing osmotic energy, respectively. Before using the real sea water and river water, the suspended solids has been filtrated using nylon support.

Supplementary Note 1: FT-IR of BNC, MoS_2 and MoS_2/BNC_3.

The FT-IR spectra of MoS_2, BNC and as-prepared MoS_2/BNC_3 are shown in Figure 2f. The pristine BNC exhibited characteristic absorption peaks at 3348, 2897, and 1061 cm^{-1} corresponding to -OH, $-CH_2$ and C−O−C stretching vibrations [2]. The Mo-S vibration peak at 468 cm^{-1} was observed in the pure MoS_2 spectrum. The peak at 3500 cm^{-1} can be attributed to the -OH peak in H_2O adsorbed by pure MoS_2[3]. The as-prepared MoS_2/BNC shows a characteristic peak of the S-H bond at 2552 cm^{-1}. Due to the instability of S-H bonds in air, the peak strength become weak. To clearly verify S-H bonds, the magnified FT-IR of MoS_2/BNC_{20} has been given in Figure S7(b).

Supplementary Note 2: The mechanical strength indictors calculation formula.

The tensile strength can be obtained From Equation (S2):

$$\sigma=\frac{F_{max}}{S} \tag{S2}$$

σ - Tensile strength, F_{max} - Maximum force, S - Cross sectional area (0.45 mm^2).

The failure stress can be obtained from Equation (S3):

$$\sigma_f=F_f/S \tag{S3}$$

σ_f - Failure stress, F_f - Failure force, S - Cross sectional area (0.45 mm^2).

The yield stress can be obtained by Equation (S4):

$$\sigma_y=F_y/S \tag{S4}$$

In which σ_y - Yield stress, F_y -Yield force (obtained from Figure 5), S - Cross sectional area (0.45 mm^2).

Supplementary Note 3: Numerical Simulation

To optimize the contribution of space charge for ion transport, the numerical model based on Poisson-Nernst-Planck and Naver-Stokes (PNP-NS) equations was built. It was assumed that the nanochannels in MoS_2/BNC composite membrane is a simple 2D channel (Figure S12). According to the property and zeta potential of the nanochannel, the interior surface charge from MoS_2 nanosheets and space charge of nanochannel from interlayered BCN is defined. For pure MoS_2 nanosheets, the surface charge is calculated to be -34 mC m^{-2} based on the zeta potential. The effect of charge on the ionic selectivity of nano-channels was theoretically calculated with the commercial finite-element software package COMSOL Multiphysics. The Numerical simulation was performed

based on coupled Poisson-Nernst-Plank and Navier-Stokes equations. The flux of each ionic species can be physically described by the Nernst-Planck equations. The ionic flux (J_i) was calculated as:[4-7]

$$J_i=-D_i\left(\nabla c_i+\frac{Z_iFc_i}{RT}\nabla\varphi\right)+c_iu \tag{S5}$$

where the three terms on the right side of equation represent ion convection, ion diffusion and ion electrochemical migration respectively. D_i is the diffusion coefficient, c_i is the ion concentration of the species i, Z_i is the charge of the species i, F is Faraday constant, R is universal gas constant and φ is the electrical potential. u is the fluid velocity controlled by Navier Stokes equation:

$$\nabla u=0 \tag{S6}$$

$$\mu\nabla^2u-\nabla p-\rho_e\nabla\varphi=0 \tag{S7}$$

where P is the pressure, μ is the dynamic viscosity and ρ_e is the charge density. The relationship between the electric potential (φ) and ion concentrations (c_i) satisfies the Poisson equation:

$$\nabla^2\varphi=-\frac{\rho_e}{\varepsilon}=-\frac{\rho_s+\rho_0}{\varepsilon} \tag{S8}$$

$$\rho_0=F\sum_i z_ic_i \tag{S9}$$

where ε is permittivity of the fluid, ρ_0 is the surface charge density of the mobile ions, ρ_s is the space charge brought by BNC. When the system reaches a steady state under steady conditions, the ion flux should satisfy a time-independent continuity:

$$\nabla\cdot J_i=0 \tag{S10}$$

The ion flux has the zero normal components at boundaries:

$$n\cdot J_i=0 \tag{S11}$$

The ionic current (I) across the reservoir and the nanochannel is calculated from:

$$I=\int_S F\left(z_pJ_p+z_nJ_n\right)\cdot ndS \tag{S12}$$

The couple equations are solved assuming appropriate boundary conditions. The model of the numerical simulations is show in Figure S6. It contains a 28 nm long 2D channel, and the size of the channel were set as 9.79 Å. To minimize the effect of the resistance of mass transfer at the entrance and exit, two electrolyte reservoirs (400 nm *300 nm) were added. Different concentrations of NaCl were set in the reservoirs on both sides. The surface charge density on the walls of the reservoir was assumed to be zero. The external potential is applied across the channel.

Supplementary Note 4: Density functional theory (DFT) Simulation

Based on density functional theory (DFT), the migration energy barriers of Na^+ and Cl^- in different structures were calculated using the Dmol^3 package of the Materials Studio 2019 software[8]. According to our experimental results, the MoS_2 membrane was constructed with the average layer spacing of 8.83 Å, and the surface was terminated by -S. The MoS_2/BNC membrane was constructed with the average layer spacing of 9.79 Å, and the channel was filled with BNC. The model is shown in Figure S12. During DFT calculation by Dmol^3 package, the exchange correlation effects were accounted by using the generalized gradient approximation of PBE employed for the exchanged-correlation functional together with the double-numerical quality basis set with polarization functions (DNP with 3.5 basis file). The electron–ion interactions were treated using the effective core potential. A 3×3×1 k-mesh was employed for the Brillouin zone integrations, and a vacuum layer of 15 Å was used to avoid possible interactions between the images. The migration energy barriers were calculated using the method of TS search with the equation of $E_a = E_{TS} - E_r$ (E_a is the energy barrier, E_{TS} is the energy of transition state, E_r is the energy of the system before migration.

Figures

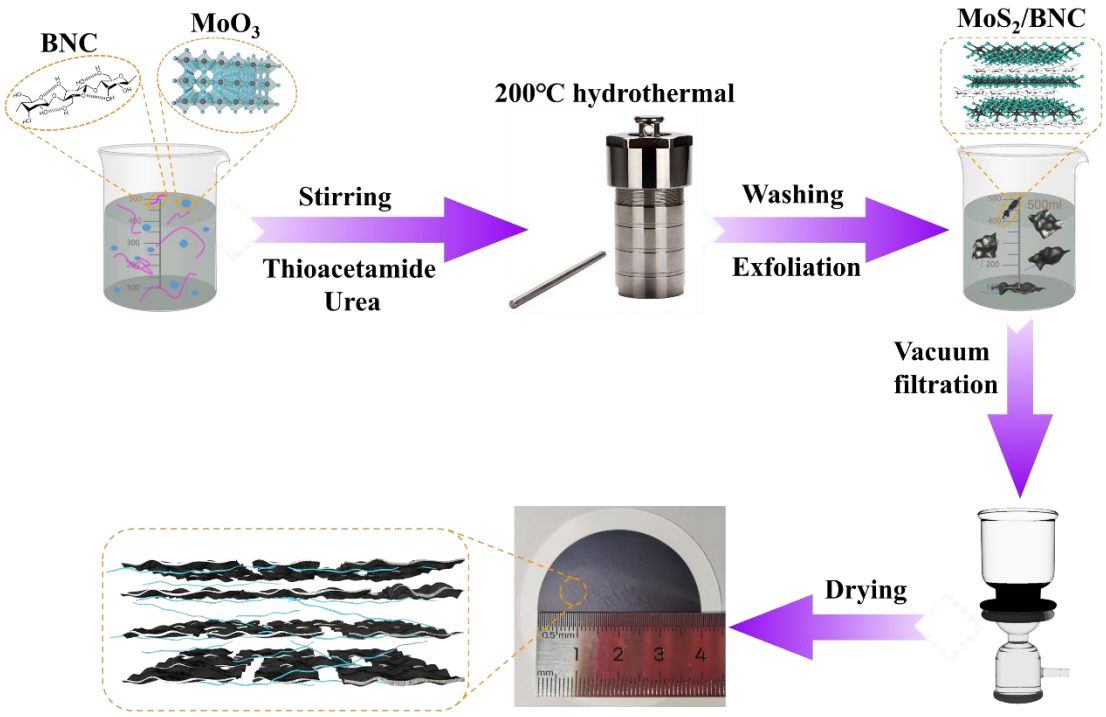

Figure S1. Schematic illustration of the fabrication process of MoS_2/BNC composite Membrane.

Note: Please refer to ***Fabrication of MoS_2/BNC composite membrane in Supporting Information***.

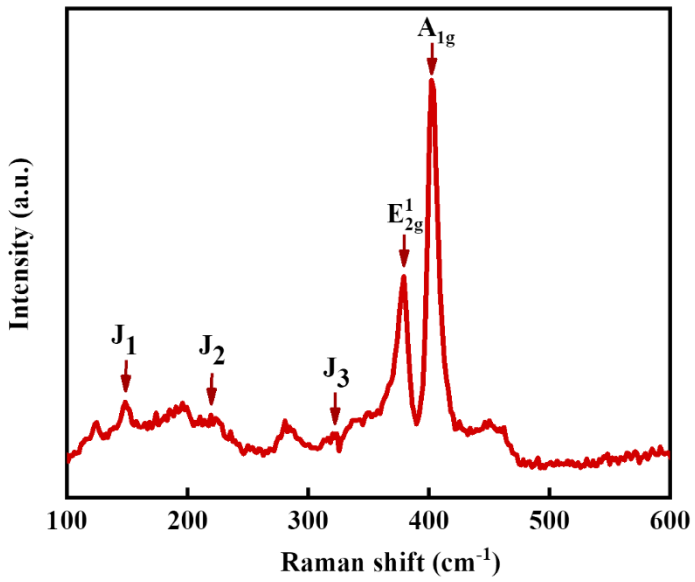

Figure S2. Raman spectra of as-prepared MoS_2.

Note: Figure S2 shows the Raman spectra of as-prepared MoS_2 by hydrothermal synthesis, in which the J_1, J_2, and J_3 phonon modes of 1T MoS_2 at 148, 224 and 322 cm^{-1} can be observed. The A_{1g} and $E_{2g}{}^1$ vibrational modes of 2H MoS_2 at 402 and 379 cm^{-1} characteristic peaks, respectively, indicate the presence of a mixture of metallic and semiconductor phases in as-prepared MoS_2.

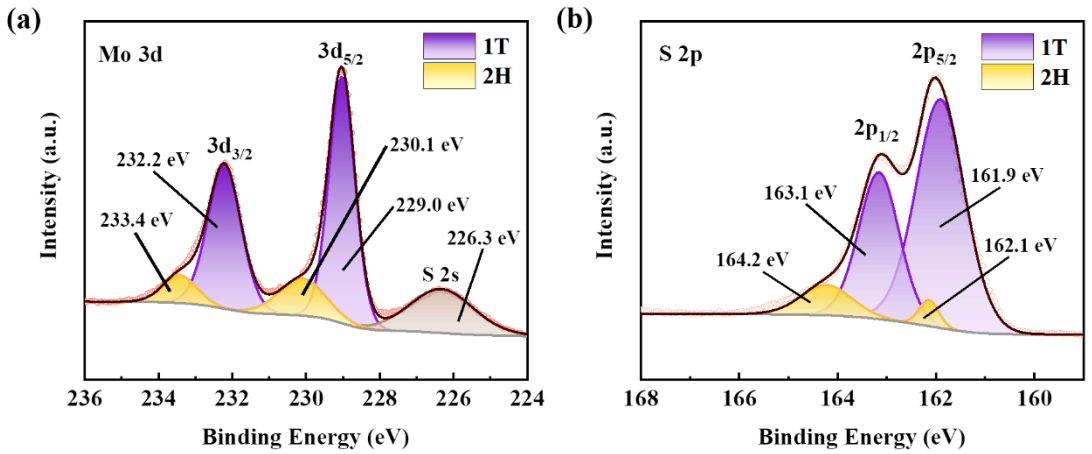

Figure S3. XPS spectrum of as-prepared MoS_2. (a) XPS spectrum of Mo 3d signal; (b) XPS spectrum of S 2p signal.

Note: Figure S3 shows the high-resolution XPS pattern of S Mo of as-prepared MoS_2. From Figure S3a, the characteristic peaks at 232.2 and 229.0 eV in the Mo 3d spectra are attributed to 1T MoS_2 Mo^{4+} $3d_{3/2}$ and Mo4+ $3d_{5/2}$, respectively. Characteristic peaks of 2H MoS_2 with binding energies of 223.4 and 230.1 eV are also observed. The S 2p spectra of Figure S3b show characteristic peaks of the 2H phase at 164.2 and 162.1 eV of the 1T phase at 163.1 and 161.9 eV, respectively. According to the deconvolution peak area calculation, the content of 1T phase in the prepared MoS_2 is obviously higher than that of 2H phase, showing the abundant 1T phase for the resultant MoS_2 materials.

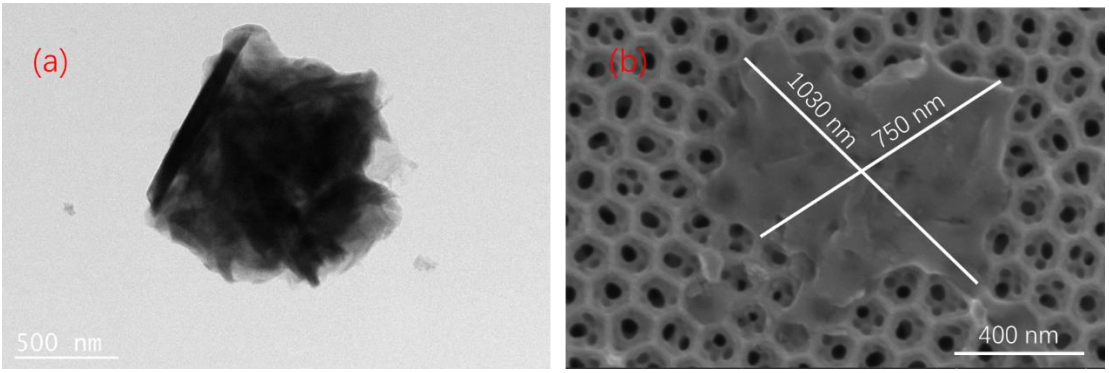

Figure S4 TEM (a) and SEM (b) images of as-prepared MoS_2 nanosheets.

Note: The flexible MoS_2 nanosheets has been obtained from Figure S4(a) inspite of the folding. After dispersion, 2D nanosheets can also be observed from Figure S4(b) on the AAO substate. This indicates the successful preparation of MoS_2 nanosheets.

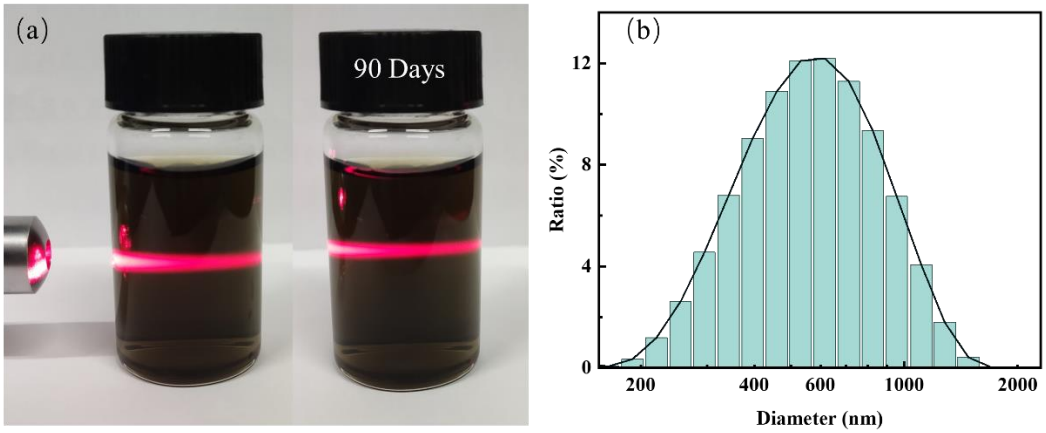

Figure S5. (a)Digital photographs of MoS_2/BNC_3 nanosheets suspended in water with Tyndall effect, and (b) particle distribution of MoS_2/BNC_3 suspension.

Note: The left side of Fig. S5(a) shows a digital photograph of the suspension in water of exfoliated MoS_2/BNC_3 nanosheets. The nanosheets were stably dispersed in water, showing a clear Tyndall effect. After 90 days on the right side, the suspension of nanosheets still shows an obvious Tyndall effect. This proves that BNC can effectively inhibits the agglomeration of MoS_2 and ensures its long-term stability. From Figure S5(b), the partical size is ~600 nm. Together with Figure S4, the 2D nanosheets can be verified for the prepared MoS_2/BNC_3 composites.

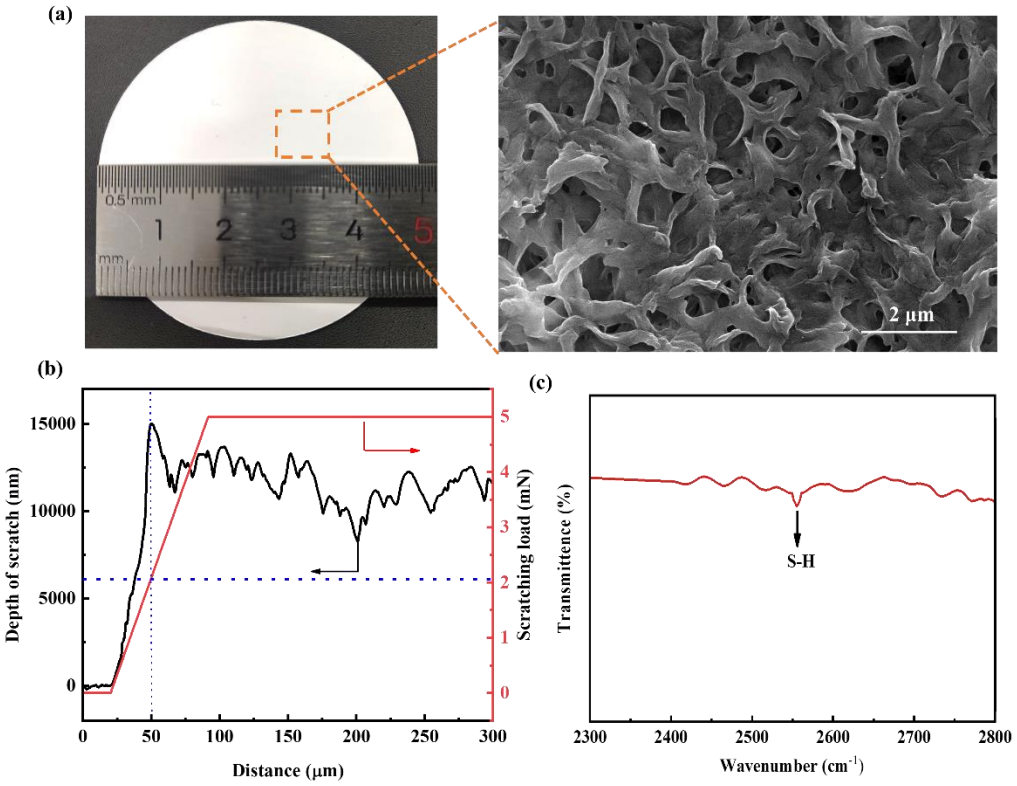

Figure S6. (a) Nylon filtration mesh digital photograph (left) and SEM images (right), (b) the combination force of functional membrane and substrate, and (c) FT-IR of MoS_2/BNC composite materials.

Note: Figure S6(a) shows the digital photograph of Nylon filtration mesh used in the experiment on the left, and the SEM image of the surface of the nylon filtration mesh with a pore size of about 0.22 μm on the right. This shows no resistance for water and ions transport in testing. From S6(b), the scratching load is about 2.1 mN, indicating the strong combination force of membrane layer and nylon substrate. From Figure S6 (c), the peak at ~2552 cm^{-1} is assigned to S-H bond, further verify the strong combination of MoS_2 and BNC.

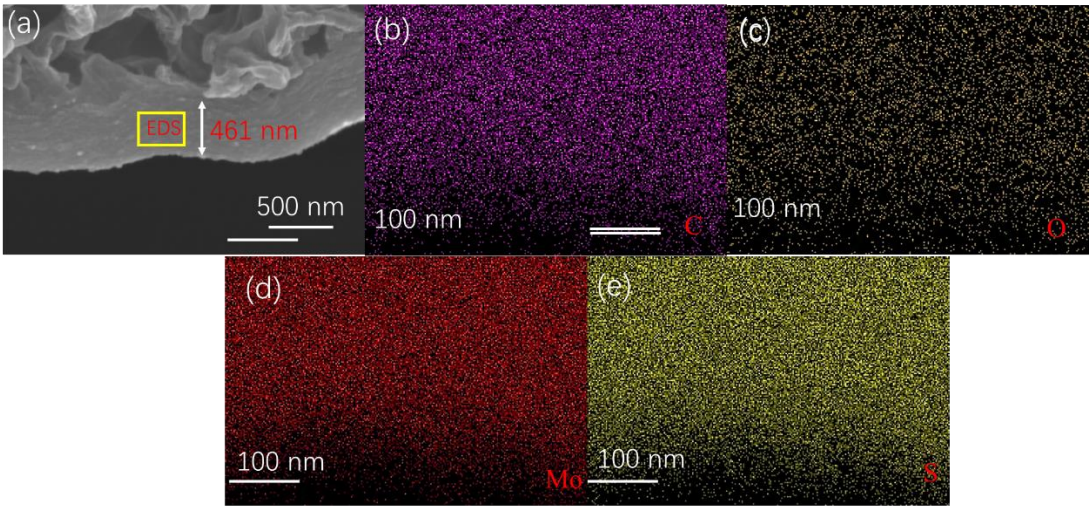

Figure S7 The SEM (a) and EDS mapping of MoS_2/BNC composite membrane (b,c,d, e).

Note: Figure S7 (a) shows the cross-section of MoS_2/BNC composite membrane with the thicknees of 461 nm. The EDS results show uniform distribution of the elments of O, C, Mo and S, indicating the sucessful preparation of MoS_2/BNC composite membrane.

To prepapre the sample for SEM analysis, the composite membarne sample was immersed inside the liquid nitrogen for a few minutes. Then the sample was quickly broken to get a good cross section for SEM observation. The observed O is sourced from the BNC. Noteworthy is that carbon film was coated on sample for SEM observation so the carbon may be sourced from the coating or BNC.

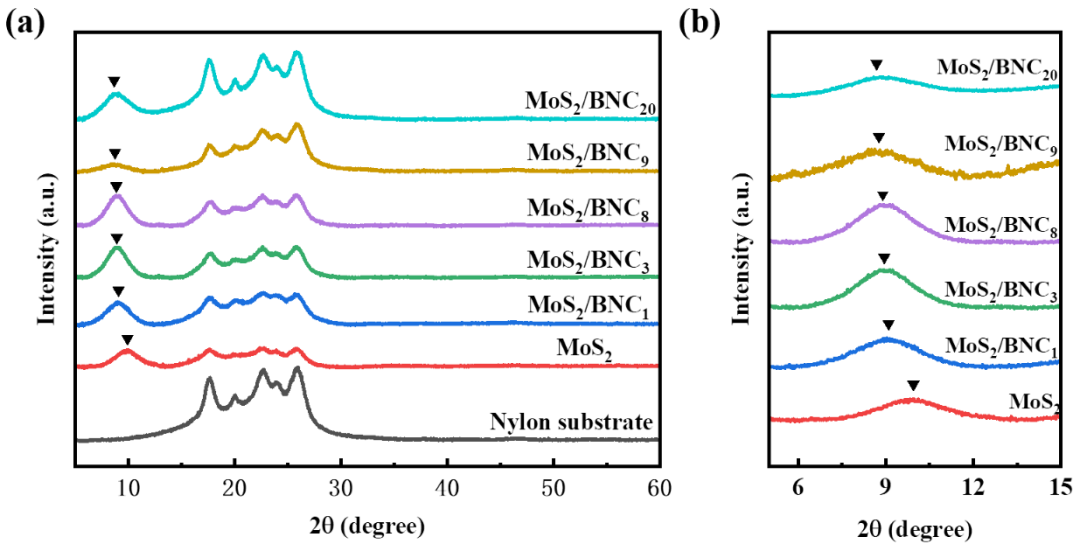

Figure S8. XRD images of the MoS_2/BNC_x membranes (a) and their magnified part(b) .

Note: Figure S8 shows the XRD images of MoS_2/BNC composite membranes with different BNC contents. The typical diffraction peaks of MoS_2-based membrane is from 10.009 to 8.621 ° with increasing BNC contents from 0 to 20 wt%. The interlayer spacing of the composite membrane can be calculated based on Bragg's equation as equation (S9) [9]:

$$2d\sin\vartheta = n\lambda \quad \text{(S9)}$$

Considering the apparatus erro of ±1% , the corresponding interlayer spacings are revised as 8.83±0.17, 9.68±0.21, 9.79±0.22, 9.86±0.22, 9.92±0.23 and 10.25±0.23 Å, respectively. This indicates the increasing interlayer spacing due to the addition of BNC.

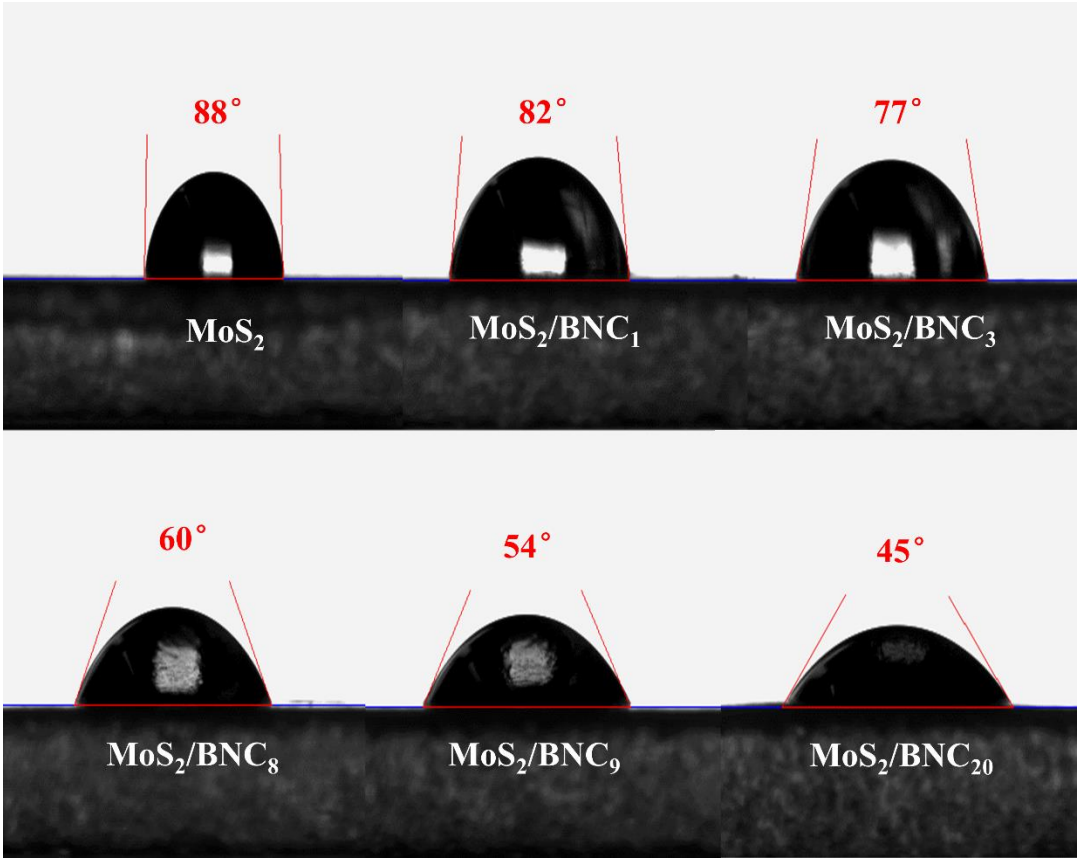

Figure S9. Contact angles of MoS_2/BNC_x composite membranes.

Note: From Figure S9, the results MoS_2/BNC_x composite membrane contact angle show that with the increase of BNC content from 0 to 20 wt%, the contact angle gradully decreases from 88˚ to 45˚. This indicates the enhancing hydrophilicity of the composite membrane, which is more conducive to water permeation.

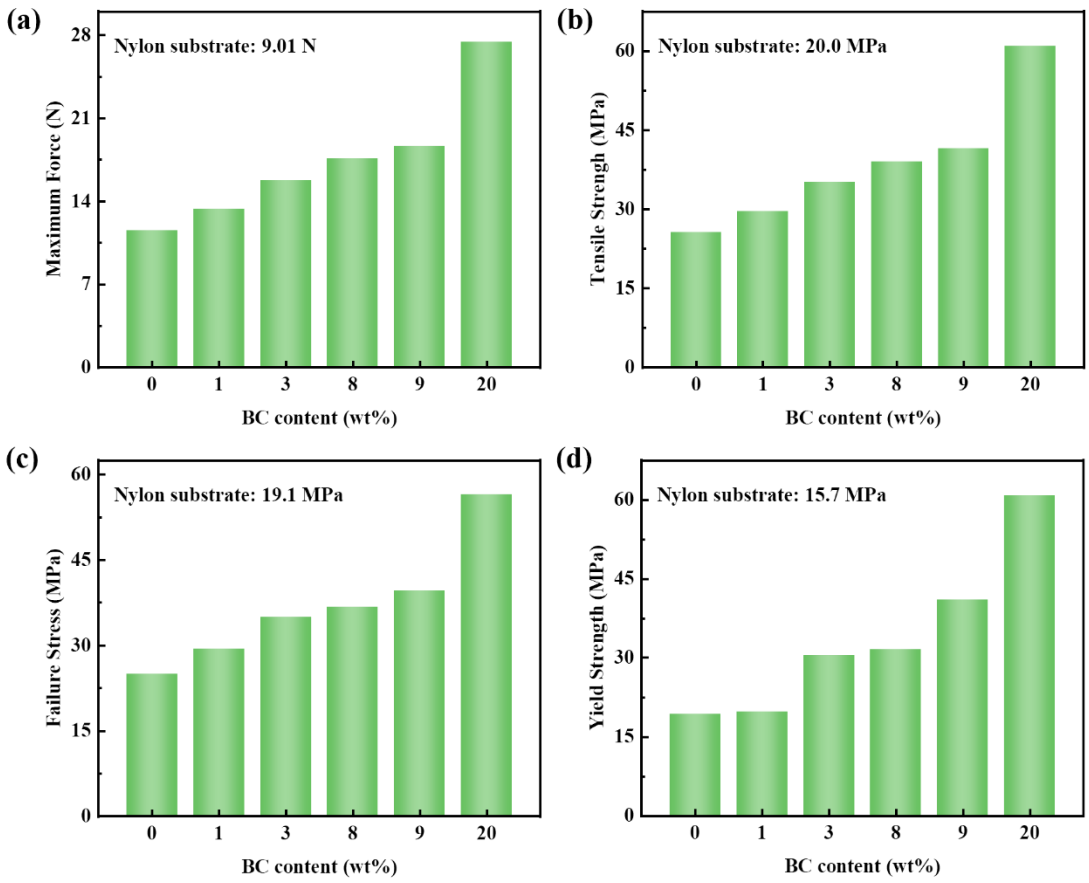

Figure S10. Tensile performance of MoS_2/BNC composite membrane with different BNC content. (a) Maximum tensile force, (b) Tensile strength, (c) Failure stress, and (d) Yield strength.

Note: From Figure S10, all the maximum tensile force, tensile strength, yield strength, and failure stress increased with the increase of BNC content. The mechanical strength of the composite membrane is obviously higher than that of the nylon substrate. The maximum bearing capacity, tensile strength, failure stress, and yield strengths of the composite membranes increase from 11.53 N to 27.41 N, 25.6 MPa to 60.9 MPa, 25 MPa to 56.5 MPa, 19.3 MPa to 60.8 MPa, respectively, with the increasing BNC content from 0, 1, 3, 8, 9 to 20 wt%, highlighting the promising application. It is worth noting that a sharp increase for 20 wt% samples is attributing to higher content of BNC, in which the formation of more network structure including S-H and hydrogen bonds between BNCs or BNC and MoS_2 nanosheets.

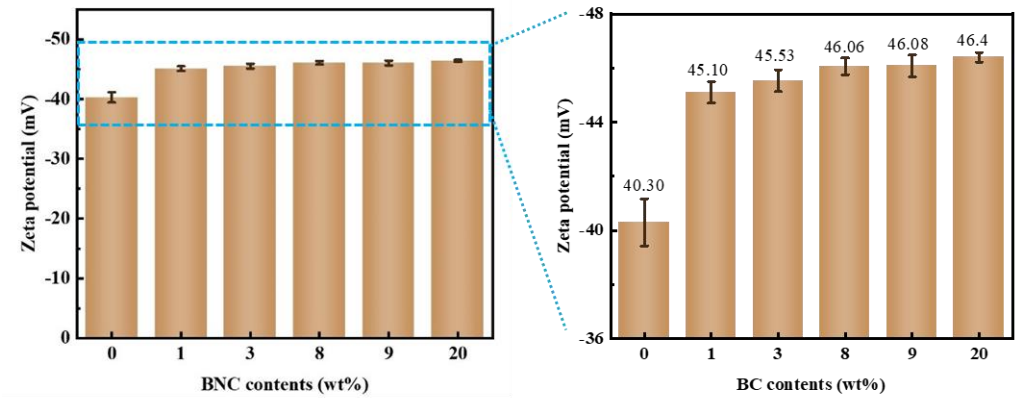

Figure S11. The zeta potential measurement of MoS_2/BNC_x materials and its mangnified part.

Note: With increasing BNC content from 0, 1, 3, 8, 9 to 20 wt%, the negativity of the MoS_2/BNCx materials effectively enhanced from -40.3 mV to 46.4 mV, facilicating the adsorption and transport of cations. This would result in higher ion selectivity and permation flux.

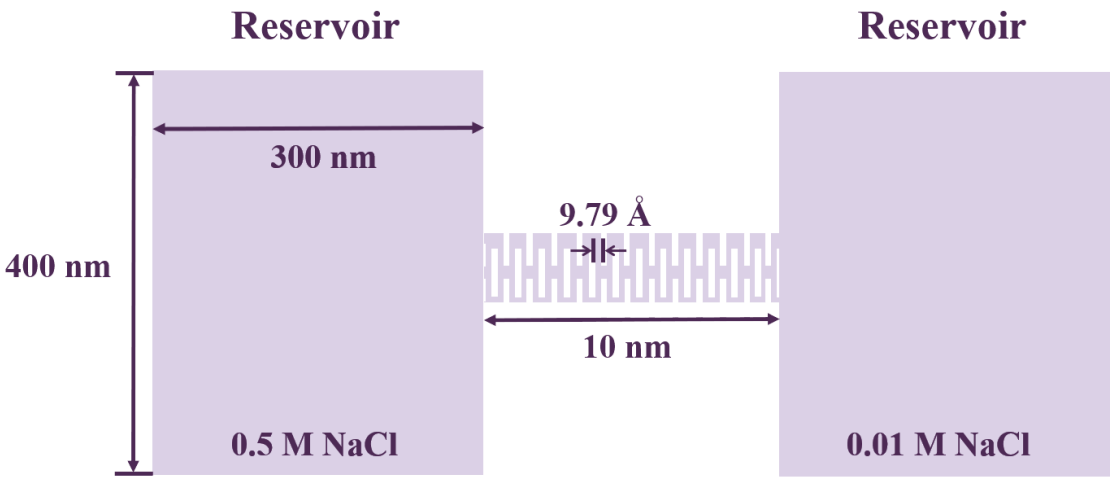

Figure S12. Model of numerical simulation.

Note: in this model, the membrane is supposed as the simple zigzag structure with a lengther of 28 nm and interlayer spacing of 9.79 Å, seperating two reservoirs with 400 nm×300 nm. One of reservior contains 0.5 M of NaCl, and another is 0.01 M of NaCl solution. This is close to the concontration gradients between sea water and water.

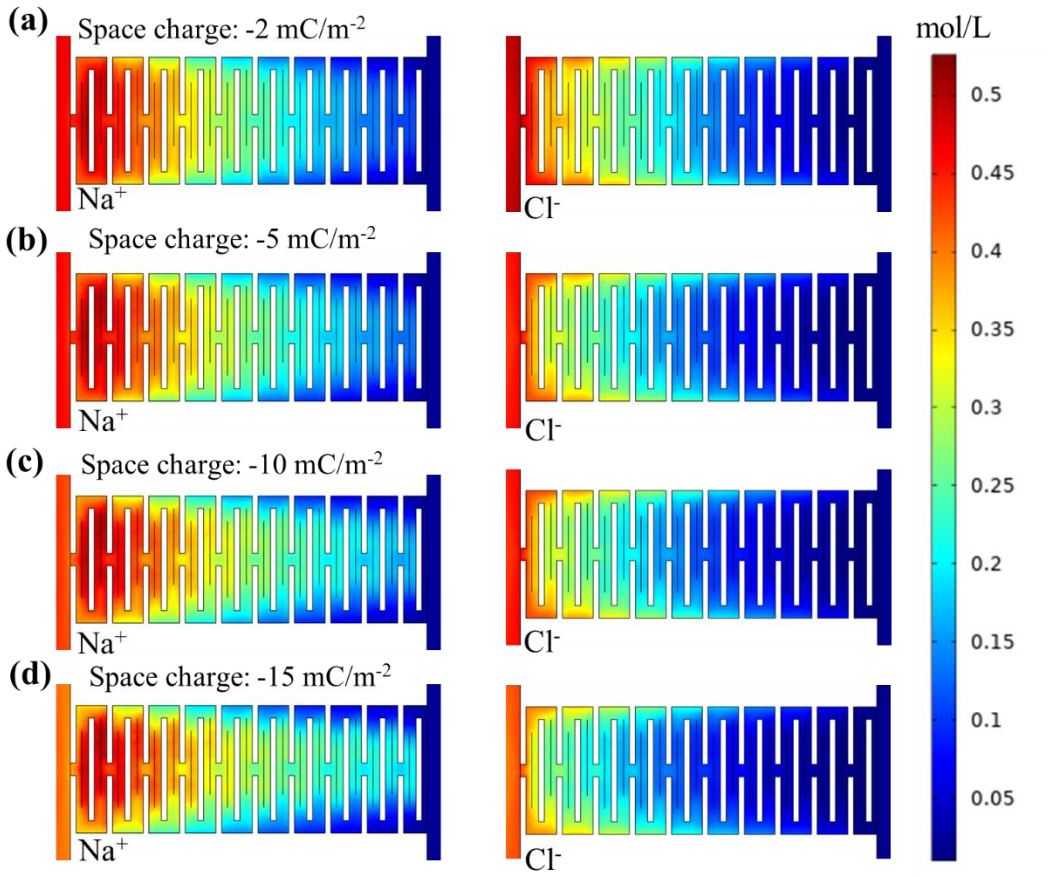

Figure S13. Simulation of different space charge densities affection ion transport. (a) -2 mC/m^{-2}, (b) -5 mC/m^{-2}, (c) -10 mC/m^{-2}, (d) -15 mC/m^{-2}.

Note: According to the simulation results in Fig. S13, the increase of space charge density in nanochannels improves the ion selectivity in the channel. However, when the space charge density in the nano-channel exceeds 10 mC m^{-2}, the phenomenon of concentration polarisation occurs in the channel, reducing the effective concentration gradient. This indicates the decrease of permeable cation, not conductive to the further improving of osmotic power. Therefore, it is required to observe the synergistic effect of space charge and surface charge for the membrane materials.

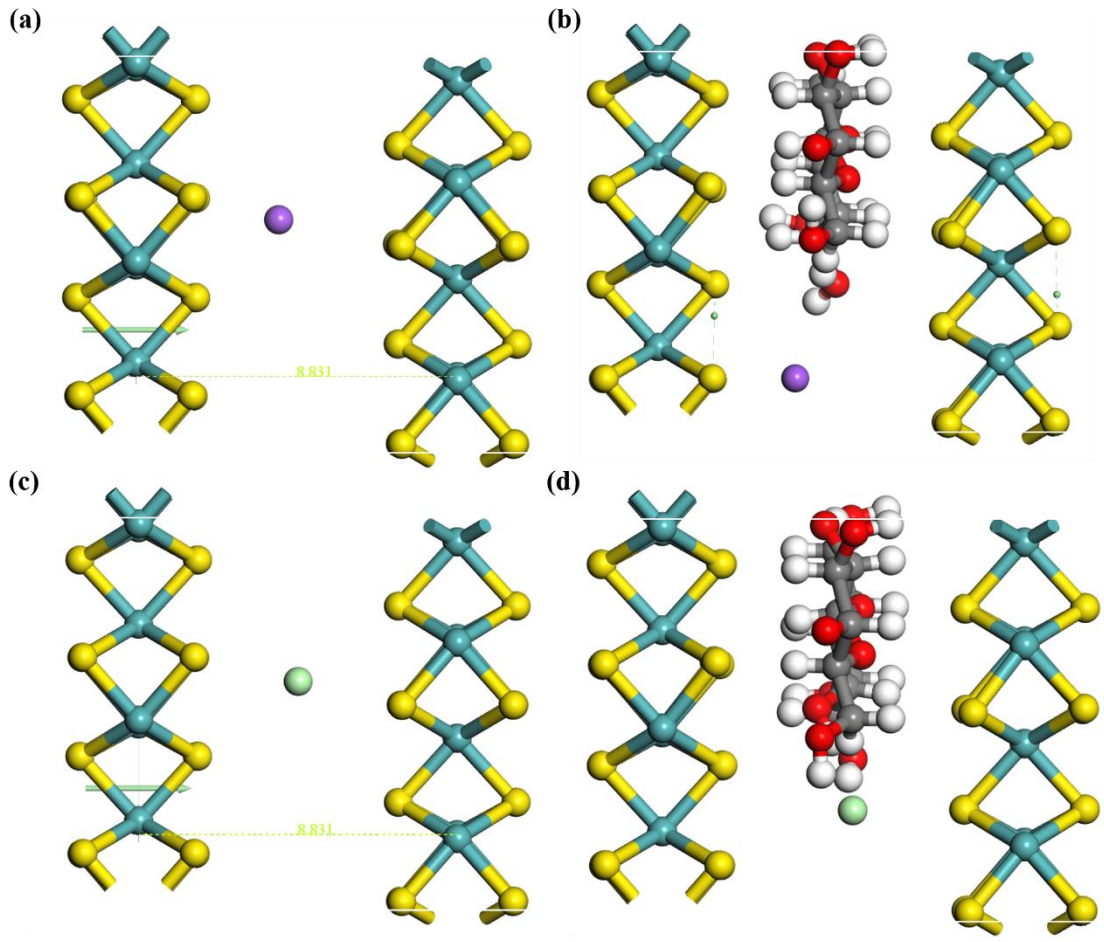

Figure S14. The schematic diagram of DFT simulation of ion migration. Na^+(purle) transport in the channel of (a) MoS_2 and (b) MoS_2/BNC. Cl^- (light green) transport in the channel of (c) MoS_2 and (d)MoS_2/BNC.

Note: please see Supplementary Note 4.

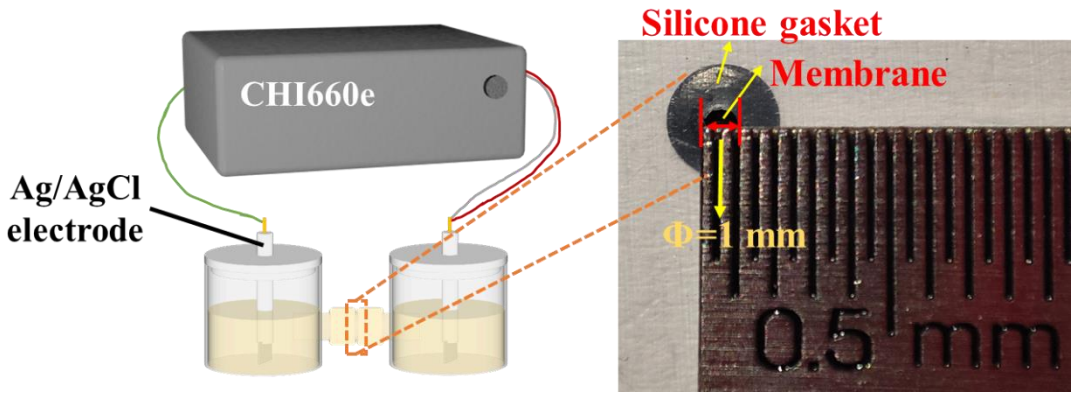

Figure S15. The schematic device in the testing.

Note: The digital photograph of the composite membrane after encapsulation with a silicone gasket is shown on the left side of Figure S15, with an effective test area of 0.78 mm^2.

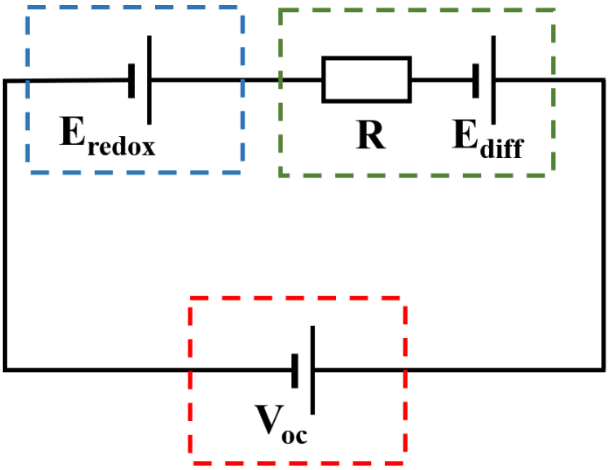

Figure S16. Equivalent circuit diagram of the osmotic energy conversion system.

Note: Figure S16 provides a detailed schematic of the modeling circuit in testing the osmotic power. The measured V_{oc} is comprised of the diffusion potential (E_{diff}) and the redox potential (E_{redox}) ($V_{oc} = E_{diff} + E_{redox}$)[10]. Eredox results from an unequal voltage drop between the electrode and electrolyte solution interface, whereas E_{diff} is induced by ion diffusion as a result of a salinity gradient.[11, 12] By deducting the contribution of the electrode redox potential, the permeation current (I_{os}) and permeation potential (V_{os}) can be further adjusted (Figure 5a), which can be used to calculate the ideal osmotic power ($P = I \times V/4$).

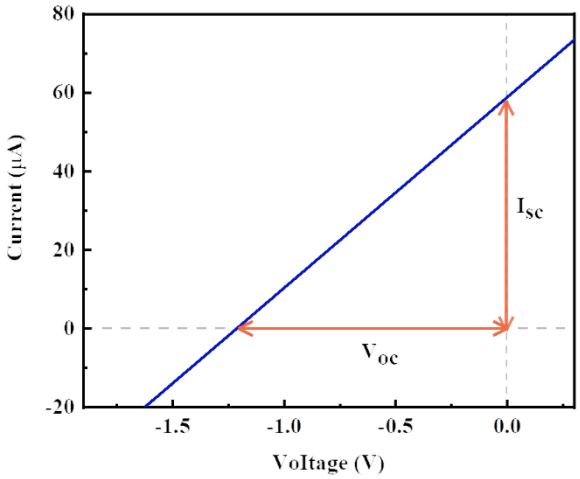

Figure S17. Under a transmembrane salinity gradient (0.01 M/0.5 M NaCl), open-circuit voltage (V_{oc}) and short-circuit current (I_{sc}) are observed.

Note: The I-V curves, measured at the transmembrane concentration gradient of the MoS_2/BNC composite membrane with a BNC content of 3 wt% (Figure S17), can be observed as open-circuit voltage (V_{oc}) and short-circuit current (I_{sc}) of 1.2 V and 58.95 μA, respectively.

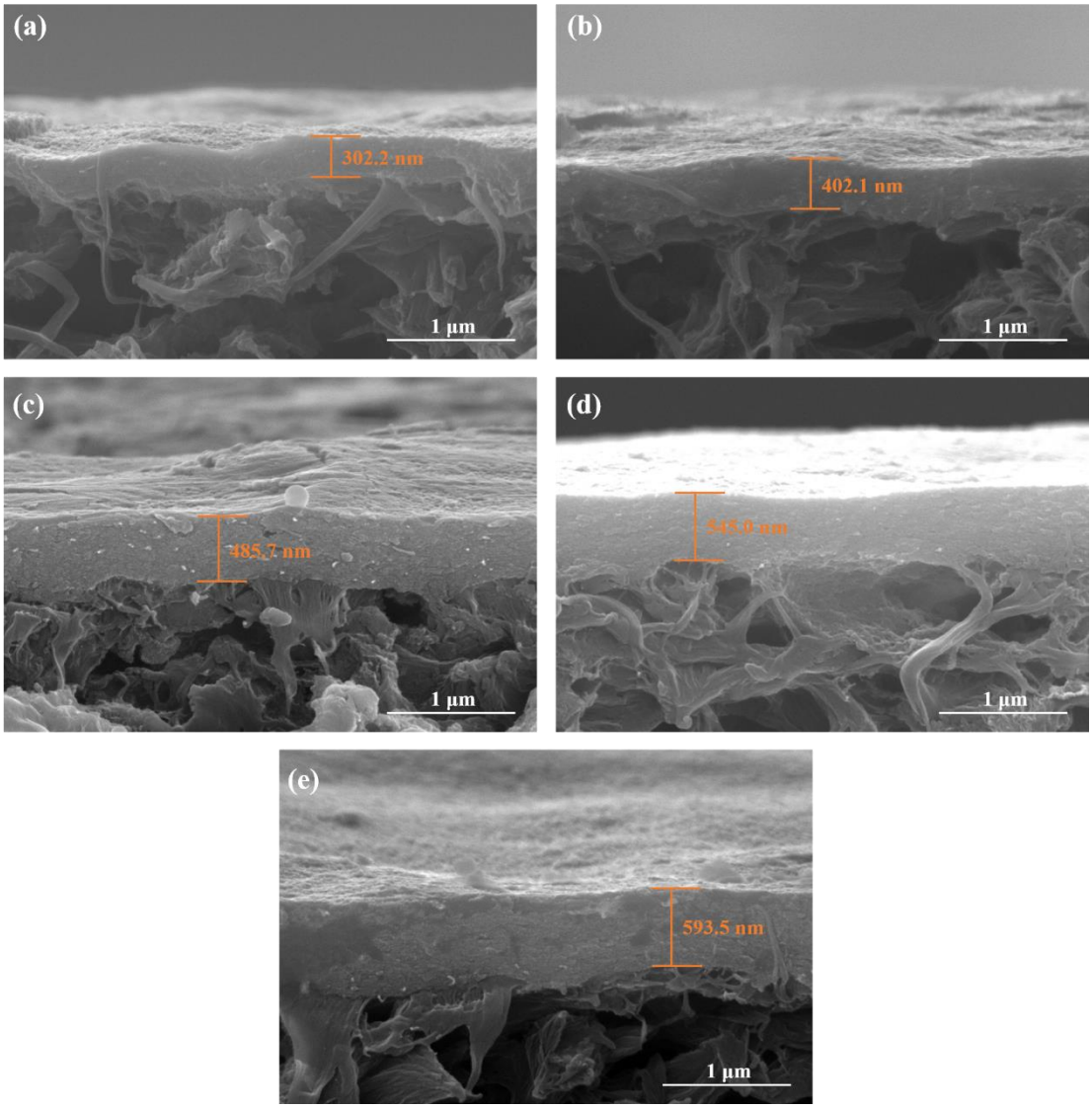

Figure S18. The SEM cross section of MoS_2/BNC_3 composite membrane with different thickness.

Note: As shown in Fig. S18, MoS_2/BNC_3 composite membranes with thicknesses of 302±5, 402±8, 485±5, 545±5, and 593± 6 nm can be obtained by controlling volumes of nanosheets suspension in the vacuum-assisted filtration process. Due to curved support, the thickness of membrane is obtained using the average value of three meansurments with error bar.

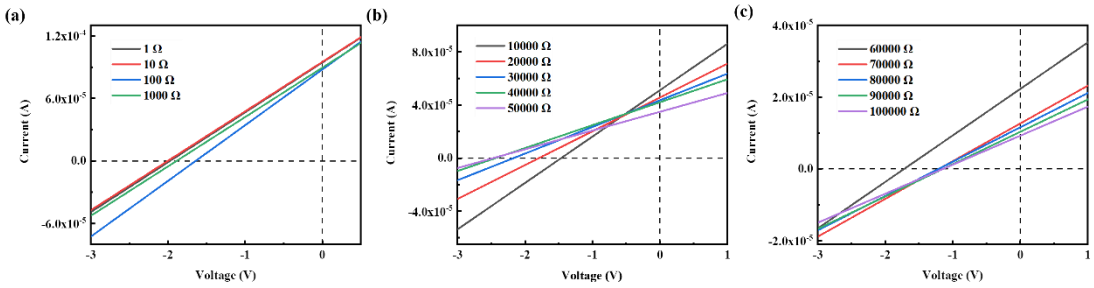

Figure.S19 *I-V* curves of MoS_2/BNC_3 composite membranes in 0.01 M/0.5 M NaCl on external loadings.

Note: A series of external resistor (R_L) connected to a flow cell module in Figure S19 can estimate the membrane resistance by testing the output *I-V* curves. The osmotic power density is based on the following equation (S13).

$$P=\frac{I^2R_L}{S} \tag{S13}$$

where *I* is the current, and *S* is membrane area, which are used to determine the osmotic power. The power density firstly increases and subsequently drops as R_L grows, whereas the current density gradually decreases.

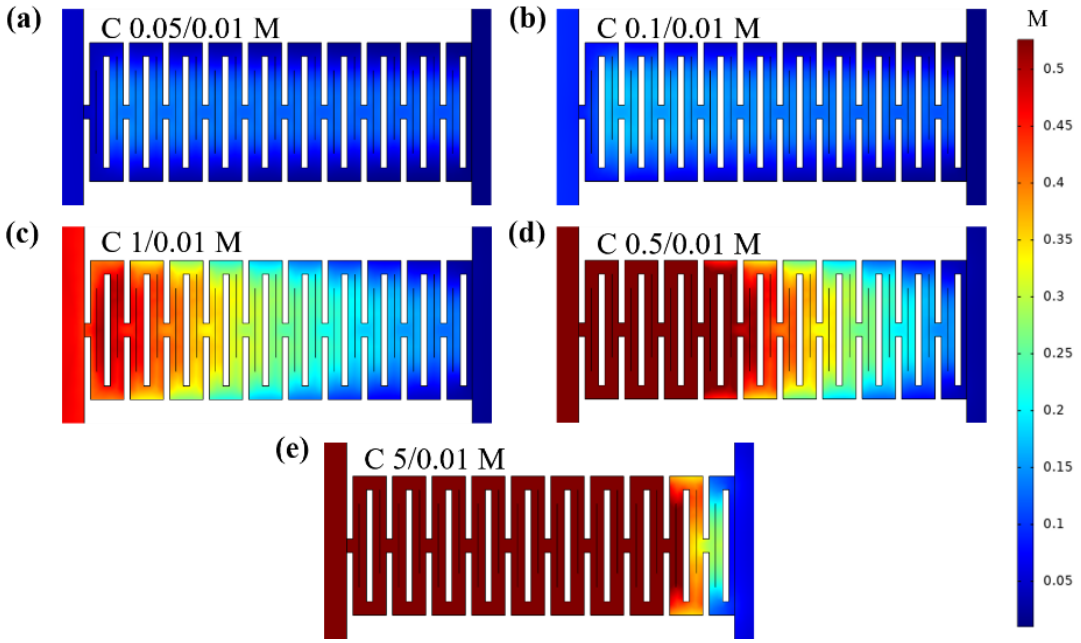

Figure S20. Schematic distribution of Na^+ in nanochannels with different concentration gradients. (a) 5-fold; (b) 10-fold; (c) 50-fold; (d) 100-fold; (e) 500-fold salinity gradient.

Note: The results of numerical simulations under different salinity gradients are shown in Figure S20. The concentration polarisation in the nanochannels is observed to be aggravated as the concentration gradient increases.

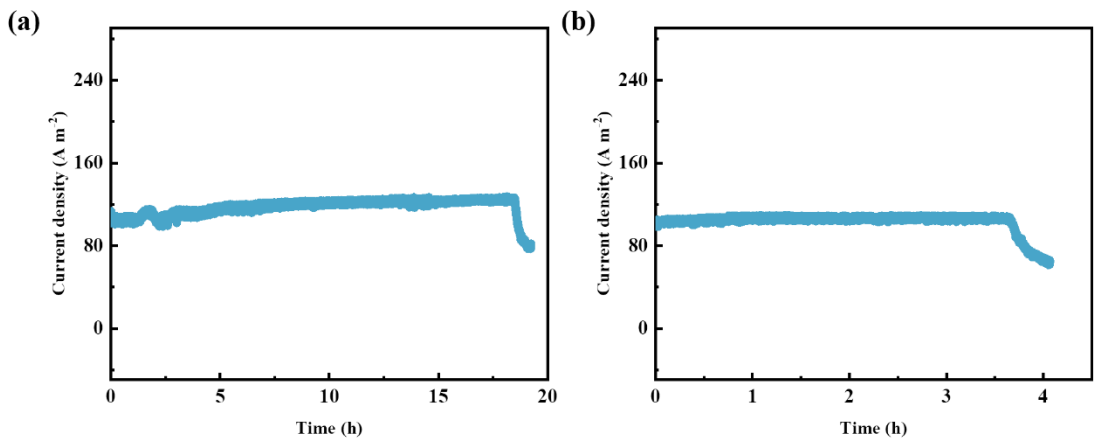

Figure S21. Stability tests of the MoS_2/BNC_3 (a) and MoS_2 (b) membrane-based device.

Note: As shown in Fig. S21, the stable duration of continuous osmotic energy conversion of the MoS_2/BNC_3 composite membrane is more than 18 hours. Pure MoS_2 membranes have a stable duration of 3.5 hours for continuous osmotic energy conversion. Obviously, the composite membrane exhibits good stability, indicating the further improving for application.

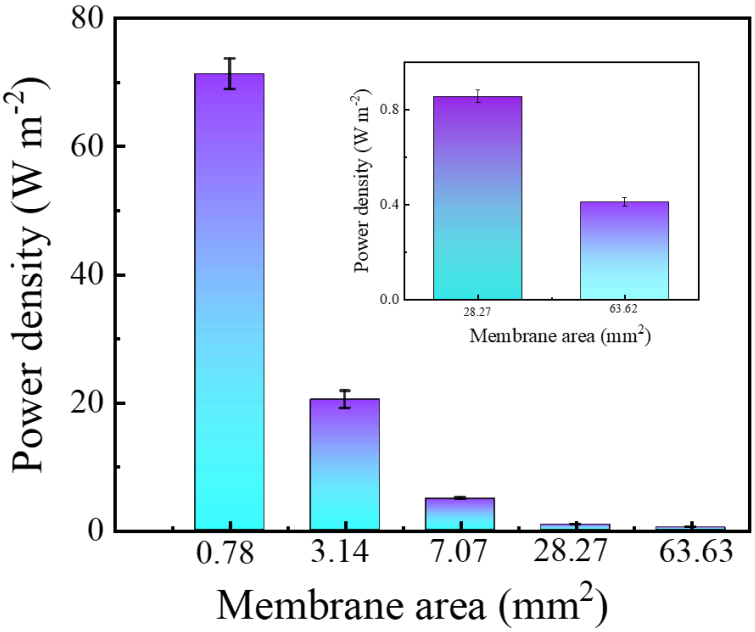

Figurre S22 The varation of power density with increasing membrane testing area.

Note: As shown in Figure S22, a sudden decrease of power density to 0.4 W m^{-2} (~63.63 mm^2) can be attributed to the combined effects: The number of co-ions in the nanoflow channel increases, counterion diffusion is hindered, and random defects increase. In addition, the ion concentration polarization is intensified due to mutual interference in transports.

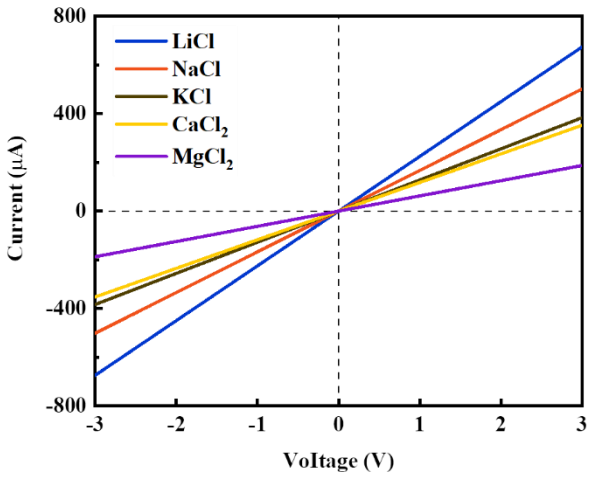

Figure S23. The effect of different electrolytes on the ionic conductivity of the membranes.

Note: Figure S23 shows the transmembrane ionic conductivity of different cations. For monovalent ions, the slope of I-V curves for Li^+ is higher than that of Na^+ and K^+, indicating higher conducting. Comparing to monovalent ions, the divalent ions have also shown lower ionic conductivities due to their stronger adsorption between interlayers resulting in shorting interlayer spacing.

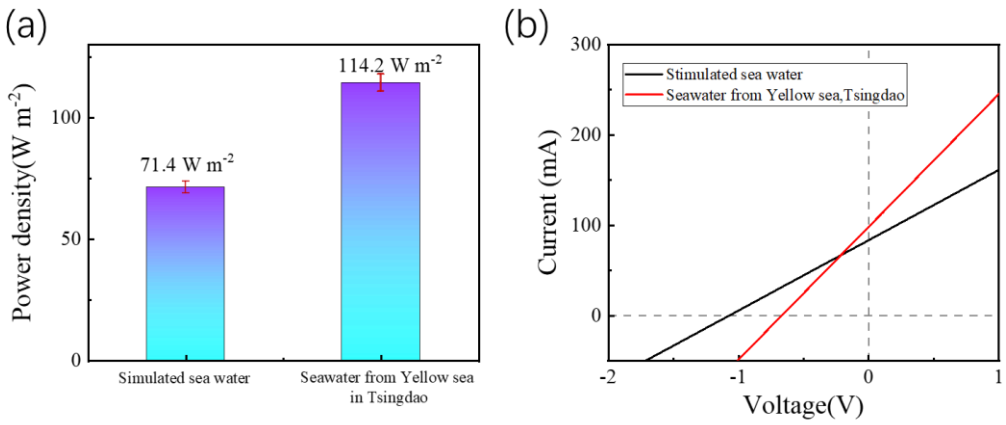

Figure S24 The power density (a) and its I-V curves (b) between seawater from Yellow Sea in Tsingdao, China .

Note: To further show the potential application, the power density has been tested using real seawater and river water. By comparison, a higher power density of 114.2 W m^{-2} based on the salinity gradients between low-salinity river water from Jixia lake in Shandong university of Technology and high-salinity seawater from Tsingdao has been obtained (Figure S24). The higher output is due to the mixed transport of other monovalent ions (Li^+, K^+ etc in seawater) and divalent ions (Ca^{2+}, Mg^{2+}), which is our future extensive exploration.

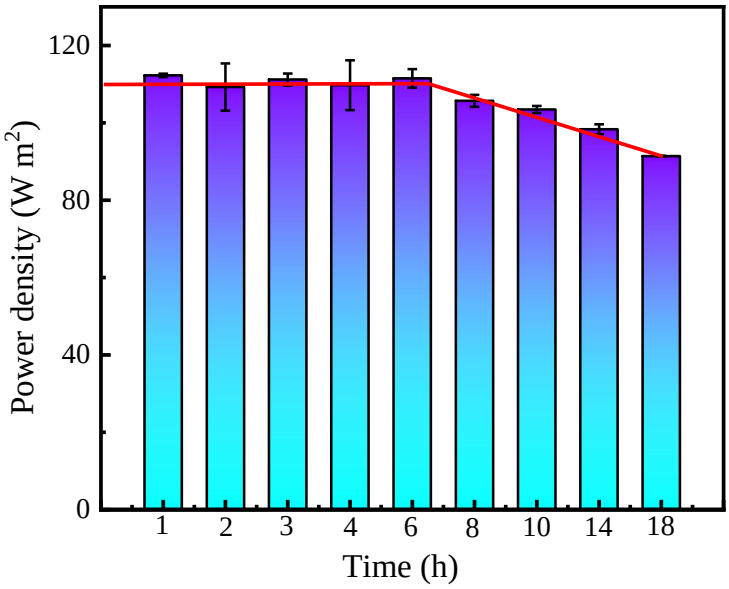

Figure S25 Stability tests of the MoS_2/BNC_3 membrane-based device under the salinity gradients between low-salinity river water from Jixia lake in Shandong university of Technology and high-salinity seawater from Yellow sea, Tsingtao, China.

Note: Figure S25 shows 6-h stable output of MoS_2/BNC_3 membrane-based device under the real salinity gradients between low-salinity river water from Jixia lake in Shandong university of Technology and high-salinity seawater from Tsingtao. Comparing with the result of Figure S21, the membrane shows excellent stability under real application. After 6-h testing, the slow decrease also refects good resistane in real seawater due to the stable confined channel of the membrane in spite of the decreasing salinity gradients. Until 18-h testing, the attenuation rate is just 8%, further verifying the promising application.

Tables

Table S1. Comparison of power density under salinity gradient using different 2D membrane.

Membrane	Testing area	Thickness	Stable time	Power density ($W\ m^{-2}$)	References
C-Mxene/C-HNF	3×10^{-2} mm^2	-	50 d	1.04	[13]
SAMM@AAO	0.004 mm^2	160 nm	14 d	6.76	[14]
PAA-cPEI	8×10^{3} μm^2	7 μm	60 d	7.5	[15]
CNC/PVA/GO	4.3×10^{-3} mm^2	45 μm	25 d	3.2	[16]
P-RC/P-CNTs & N-RC/N-CNTs	3.8×10^{-2} mm^2	-	50 d	5.28	[17]
GO@IL	3×10^{4} μm^2	12 μm	6000 s	6.7	[9]
V-NbP	3×10^{4} μm^2	7.4 μm	90 d	10.7	[18]
RCNFs	0.011 mm^2	-	43 d	2.75	[19]
TpEB@TpPa-SO_3Na	3×10^{4} μm^2	500 nm	30 d	20.2	[20]
N-$Ti_3C_2T_x$/P-$Ti_3C_2T_x$	3×10^{4} μm^2	3.5 μm	150 min	16	[11]
KCNF/Mxene	0.2 mm^2	2.83 μm	6000 s	10.56	[21]
ABN_{30}	3.14 mm^2	1 μm	10 h	0.6	[22]
VMT-PVDF	-	30 nm	216 h	30	[23]
MoS_2/CNF	3×10^{4} μm^2	4 μm	-	6.7	[24]
Nanoporous MXene	2.5×10^{-2} mm^2	9.26 μm	100 h	9.5	[25]
CNF/GO	3×10^{4} μm^2	40 μm	-	7.67	[26]
BHMXM	3×10^{4} μm^2	4 μm	20 d	8.6	[10]
COF-$(SO_3Na)_1$/PAN	-	53 nm	-	8.2	[27]
PES-SO_3H	3×10^{4} μm^2	30 mm	-	6.2	[28]
p-MOF-AAO	0.126 mm^2	500 nm	-	6.26 (3000-fold)	[29]

DAC-$Ti_{0.87}O_2$	3×10^4 μm^2	20μm	7 d	17.8	[30]
CS/SA	3×10^4 μm^2	35 mm	-	7.87	[31]
HENM	3×10^4 μm^2	40μm	-	12.34	[32]
UFSCNM	-	250 nm	-	0.21	[33]
UiO-66-NH2@ANM	3×10^4 μm^2	750 nm	7 d	26.8	[34]
polymer/MOF	3×10^4 μm^2	1.6 μm	30 d	2.87	[35]
COF	0.01 mm^2	53 nm	21 d	97	[36]
O-MXene	3×10^4 μm^2	9.2 μm	10 h	21.7	[37]
MoS_2/BNC_3	0.78 mm^2	468 nm	40 d	73	This work

References

1. F. S. Zhang, L. J. Yu, J. C. Liu, L. L. Hou, S. H. Li, H. Y. Chai, H. Li, Z. R. Xin, Q. Z. Li, Z. M. Cui, N. Wang, L. Jiang and Y. Zhao, Chemical Engineering Journal, 2022, 435, 135159.
2. G. M. Zhang, G. K. Chen, M. Dong, J. Nie and G. P. Ma, Acs Applied Materials & Interfaces, 2023, 15, 32903-32915.
3. H. Y. Shen, C. Y. Jiang, W. Li, Q. F. Wei, R. A. Ghiladi and Q. Q. Wang, Acs Applied Materials & Interfaces, 2021, 13, 31193-31205.
4. D. Wang, Z. Wang, J. Chen, H. Zhi, Y. Liu, J. Tang, N. Li, Y. Zhang, M. An, H. Liu and G. Xue, Advanced Energy Materials, 2023, 14, 232262.
5. Y.-S. Su, A. R. Fauziah, C.-Y. Wong, T.-Y. Huang and L.-H. Yeh, Small Science, 2023, 14, 232262.
6. F. K. Wang, Z. Y. Wang, X. X. Meng, X. Y. Wang, Y. Y. Fan, Y. Jin, W. M. Zhang and N. T. Yang, Journal of Membrane Science, 2023, 686, 121975.
7. R. N. Qin, J. D. Tang, C. R. Wu, Q. Q. Zhang, T. L. Xiao, Z. Y. Liu, Y. H. Jin, J. B. Liu and H. Wang, Nano Energy, 2022, 100, 107526.
8. J. Xia, H. Gao, S. Pan, T. Huang, L. Zhang, K. Sui, J. Gao, X. Liu and L. Jiang, ACS Nano, 2023, 17, 25269-25278.
9. Y. Hu, H. Xiao, L. Fu, P. Liu, Y. Wu, W. Chen, Y. Qian, S. Zhou, X. y. Kong, Z. Zhang, L. Jiang and L. Wen, Advanced Materials, 2023, 35¸2301285.
10. L. Ding, M. Zheng, D. Xiao, Z. Zhao, J. Xue, S. Zhang, J. Caro and H. Wang, Angewandte Chemie International Edition, 2022, 61, e202206152.
11. J. Wang, L. Wang, N. Shao, M. He, P. Shang, Z. Cui, S. Liu, N. Jiang, X. Wang and L. Wang, Chemical Engineering Journal, 2023, 452¸139531.
12. M. Chen, K. Yang, J. Wang, H. Sun, X. H. Xia and C. Wang, Advanced Functional Materials, 2023, 33¸2302427.
13. J. Rao, Z. Lv, X. Yan, J. Pan, G. Chen, B. Lü and F. Peng, Advanced Functional Materials, 2023, 34¸202309869.

14. J. Xiao, M. Cong, M. Li, X. Zhang, Y. Zhang, X. Zhao, W. Lu, Z. Guo, X. Liang and G. Qing, Advanced Functional Materials, 2023, 34, 2307996.
15. T. Huang, X. N. Kan, J. L. Fan, H. F. Gao, L. Yu, L. Zhang, J. X. Xia, J. Gao, X. L. Liu, K. Y. Sui and L. Jiang, Acs Nano, 2023, 17, 17245-17253.
16. X. Zhang, M. Li, F. Zhang, Q. Li, J. Xiao, Q. Lin and G. Qing, Small, 2023, 19, 23040603.
17. B. L. Zhou, Z. W. Lin, Z. J. Xie, X. T. Fu, Z. H. Yuan, C. L. Jiao, X. Z. Qin and D. D. Ye, Nano Energy, 2023, 115¸108693.
18. J. Safaei, Y. F. Gao, M. Hosseinpour, X. Y. Zhang, Y. Sun, X. Tang, Z. J. Zhang, S. J. Wang, X. Guo, Y. Wang, Z. Chen, D. Zhou, F. Y. Kang, L. Jiang and G. X. Wang, Journal of the American Chemical Society, 2023, 145, 2669-2678.
19. B. Zhou, J. Zou, Z. Lin, Z. Yuan, X. Qin, P. Chen and D. Ye, Chemical Engineering Journal, 2023, 457, 141167.
20. L. Cao, I. C. Chen, X. W. Liu, Z. Li, Z. Y. Zhou and Z. P. Lai, Acs Nano, 2022, 16, 18910-18920.
21. R. Zhai, L. Jiang, Z. Chen, X. Zhang, J. Zhou, X. Ma, C. Teng, Y. Zhou and L. Jiang, Advanced Functional Materials, 2023, 2313914
22. C. Chen, D. Liu, L. He, S. Qin, J. Wang, J. M. Razal, N. A. Kotov and W. Lei, Joule, 2020, 4, 247-261.
23. J. Wang, Z. Cui, S. Li, Z. Song, M. He, D. Huang, Y. Feng, Y. Liu, K. Zhou, X. Wang and L. Wang, Nature Communications, 2024, 15, 608.
24. C. Zhu, P. Liu, B. Niu, Y. Liu, W. Xin, W. Chen, X.-Y. Kong, Z. Zhang, L. Jiang and L. Wen, Journal of the American Chemical Society, 2021, 143, 1932-1940.
25. S. Hong, J. K. El-Demellawi, Y. Lei, Z. Liu, F. A. Marzooqi, H. A. Arafat and H. N. Alshareef, ACS Nano, 2022, 16, 792-800.
26. Q. Luo, P. Liu, L. Fu, Y. Hu, L. Yang, W. Wu, X.-Y. Kong, L. Jiang and L. Wen, ACS Applied Materials & Interfaces, 2022, 14, 13223-13230.
27. X. Zuo, C. Zhu, W. Xian, Q. W. Meng, Q. Guo, X. Zhu, S. Wang, Y. Wang, S. Ma and Q. Sun, Angewandte Chemie International Edition, 2022, 61¸e2021116910.
28. Y. Sun, T. Dong, C. Lu, W. Xin, L. Yang, P. Liu, Y. Qian, Y. Zhao, X. Y. Kong, L. Wen and L. Jiang, Angewandte Chemie International Edition, 2020, 59, 17423-17428.
29. Z. Q. Li, G. L. Zhu, R. J. Mo, M. Y. Wu, X. L. Ding, L. Q. Huang, Z. Q. Wu and X. H. Xia, Angewandte Chemie International Edition, 2022, 61, e202202698.
30. C. Liu, C. Ye, T. Zhang, J. Tang, K. Mao, L. Chen, L. Xue, J. Sun, W. Zhang, X. Wang, P. Xiong, G. Wang and J. Zhu, Angewandte Chemie International Edition, 2024, 136¸.e202315947
31. G. Bian, N. Pan, Z. Luan, X. Sui, W. Fan, Y. Xia, K. Sui and L. Jiang, Angewandte Chemie International Edition, 2021, 60, 20294-20300.
32. H. Ling, W. Xin, Y. Qian, X. He, L. Yang, W. Chen, Y. Wu, H. Du, Y. Liu, X. Y. Kong, L. Jiang and L. Wen, Angewandte Chemie International Edition, 2022, 62,e2022120.
33. K. Xiao, P. Giusto, L. Wen, L. Jiang and M. Antonietti, Angewandte Chemie International Edition, 2018, 57, 10123-10126.
34. Y.C. Liu, L.H. Yeh, M.J. Zheng and K. C. W. Wu, Science Advances, Sci. Adv. 2021; 7 : eabe9924.
35 R. Li, J. Jiang, Q. Liu, Z. Xie and J. Zhai, Nano Energy, 2018, 53, 643-649.

36 Z. Ren, Q. Zhang, J. Yin, P. Jia, W. Lu, Q. Yao, M. Deng, Y. Gao and N. Liu, Advanced Functional Materials, 2024, 2404410.

37. X. Zuo, C. Zhu, W. Xian, Q. W. Meng, Q. Guo, X. Zhu, S. Wang, Y. Wang, S. Ma and Q. Sun, Angewandte Chemie International Edition, 2022, 61, e202116910.